Electronic Supplementary Material (ESI) for Nanoscale.

Supporting information of

Mechanical Deformation induced Charge Redistribution to Promote the High Performance of Stretchable Magnesium-Ion Batteries Based on Two-Dimensional C_2N Anodes

Donghai Wu[a], Baocheng Yang[a], Houyang Chen[b*], Eli Ruckenstein[b]

[a] *Henan Key Laboratory of Nanocomposites and Applications, Institute of Nanostructured Functional Materials, Huanghe Science and Technology College, Zhengzhou 450006, China*

[b] *Department of Chemical and Biological Engineering, University at Buffalo, The State University of New York, Buffalo, New York 14260-4200, USA*

* To whom correspondence should be addressed. Email: hchen23@buffalo.edu

Section S1. Computational details

All density functional theory (DFT) computations were performed by adopting the projector augmented wave (PAW)[1] method and generalized gradient approximation (GGA) functional with the form of Perdew-Burke-Ernzerhof (PBE).[2] Calculations are implemented in the Vienna *ab-initio* simulation package (VASP).[3] The van der Waals correction was considered by adopting the DFT-D2[4] approach. The cutoff energy for the plane-wave basis set is 500 eV. The Brillouin-zone (BZ) integration is sampled with a Γ centered k-point grid of 9 × 9 × 1 for structural relaxation. The convergence thresholds of electronic self-consistent is 10^{-5} eV and of the Hellmann-Feynman force on each particle was reduced to 10^{-2} eV $Å^{-1}$ or below.

A vacuum layer (≥20 Å in the vertical direction) is employed to avoid the artificial interaction between two neighboring monolayers. The climbing-image nudged elastic band (CI-NEB) method[5] was used to optimize the energy path for the migration of Mg ions on C_2N. The Bader charge[6] integration was adopted to count the amount of charge transfer between Mg and C_2N. The stability of C_2N with maximum adatoms (2 × 2 × 1 supercell) was evaluated through *ab-initio* molecular dynamics (AIMD) simulations, with a time step of 1 fs for 5000 steps at 300 K.

Section S2. Adsorption of Mg atoms on a C_2N monolayer and stress-strain relationship of C_2N

One of the preconditions to be an anode material is that the metal atoms can be adsorbed on it. Based on the symmetry, ten possible sites for Mg adsorption (Figure S1) are considered. However, only three sites (A, B, and C sites) retain after the structural optimization. Later, the adsorption energy E_{ads} is computed by

$$E_{ads} = (E_{Mg_xC_2N} - E_{C_2N} - xE_{Mg})/x \quad \text{(S1)}$$

where $E_{Mg_xC_2N}$ and E_{C_2N} are the total energies of a C_2N monolayer with and without adsorption of Mg atoms, E_{Mg} is the energy per atom for a hexagonal close-packed Mg bulk, and x is the number of Mg adatoms. Calculated E_{ads} are -2.495, 1.751, and 1.712 eV for A, B, and C sites, respectively, implying that A sites are the most stable adsorption sites while the B and C sites cannot steadily adsorb the Mg atoms. This is different from the case of C_2N-Li/Na systems, where Li or Na atoms could be adsorbed on the top of the center of a C_4N_2 hexagon (B site) stably.

To better understand the effect of strain for the performance of stretchable batteries, we also calculate the stress-strain curves of C_2N with biaxial strains. It is found that the C_2N sheet can endure a strain as high as 16% and 11% under biaxial compressive and tensile strains (Figure S3), respectively. These large fracture strains suggest that the C_2N anode is able to accommodate the volume changes during magnesiation/demagnesiation process and further verify the good cycling stability.[7, 8] In addition, the Young's modulus of C_2N monolayer is 72.55 GPa (i.e. 145.10 N/m), which is larger than that of MoS_2 (120 N/m)[9] but is smaller than those of graphene (340 ± 50 N/m)[10] and *h*-BN (267 N/m)[11]. The calculated elastic constants of C_2N are 79.21 GPa (i.e.158.43 N/m), 22.42 GPa (i.e. 44.83 N/m), and 28.40 GPa (i.e. 56.80 N/m) for C_{11} (equal to C_{22}), C_{12}, and C_{66}, respectively, which meet the mechanical stability criteria ($(C_{11}C_{22} - C_{12}^2) > 0$ and $C_{66} > 0$) for 2D materials,[12] implying the C_2N monolayer is mechanically stable. The in-plane Young's modulus (E) and Poisson's ratio (ν) can also be derived from the elastic constants. Using the formula of $E = \left(C_{11}^2 - C_{12}^2\right)/C_{11}$ and $\nu = C_{12}/C_{11}$, the Young's modulus and Poisson's ratio are 72.87 GPa (i.e. 145.74 N/m) and 0.283, respectively. The calculated Young's modulus

from elastic constants is consistent with the result obtained by fitting the stress–strain curves.

Besides, the phonon dispersion curves of the C_2N monolayer with and without external strains are also calculated to examine the dynamic stability. As an example, no imaginary frequencies appearing in the Brillouin zone indicates that the C_2N is not only dynamically stable in the strain-free state, but also stable in dynamics under a biaxial tensile of 10% (Figure S4).

Section S3. Specific Capacity

We compute the specific capacity C via $C = xn\mathrm{F}/M$, where n, F(=26801 mA h mol^{-1}) and M are the valence of Mg^{2+} in the electrolyte, Faraday constant and molar mass of a C_2N monolayer.

Section S4. Zero point energy (ZPE) and quantum mechanical tunneling (QMT) effects

The classical and quantum diffusion rates are taken into account. Considering the harmonic approximation for vibrational modes, the transition state theory can provide an equation[13-15] for the calculation of the classic rate constant of Mg ion diffusion, i.e.,

$$k_{\mathrm{c}}^{\mathrm{TST}} = \frac{k_{\mathrm{B}} T Q^{\mathrm{TS}}}{h Q^{\mathrm{IS}}} e^{-\Delta E / k_{\mathrm{B}} T} \qquad \text{(S1)}$$

where k_B is the Boltzmann constant, T is the temperature and h represents the Planck's constant. ΔE is the classic energy barrier computed from the CI-NEB method without zero point energy (ZPE) corrections. Considering the vibrational frequencies of IS and TS (denoted as ν_i^{IS} and ν_i^{TS} , respectively), the ratio of the partition functions of the transition state (TS) and initial state (IS) (denoted as Q^{TS} and Q^{IS},

respectively) can be written by[14, 15]

$$\frac{Q^{\mathrm{TS}}}{Q^{\mathrm{IS}}}=\frac{h}{k_{\mathrm{B}}T}\frac{\prod_{i}^{3N-6}\nu_{i}^{\mathrm{IS}}}{\prod_{i}^{3N-7}\nu_{i}^{\mathrm{TS}}} \qquad \text{(S2)}$$

For the classic energy barrier, the ZPE correction (δE_{ZPE}), which is available at low temperatures, can be given by [14-16]

$$\delta E_{\mathrm{ZPE}}=\sum_{i}\frac{h\nu_{i}^{\mathrm{TS}}}{2}-\sum_{i}\frac{h\nu_{i}^{\mathrm{IS}}}{2} \qquad \text{(S3)}$$

where the first and second terms represent the total ZPE of the transition and initial states, respectively.

Comparing with ZPE correction, which is more accurate only at low temperature when the vibrational modes are in their ground states, in the classic energy barrier, the Wigner zero point correction (δE_{Wig})[17], which works better at the intermediate temperatures, can be described[17]

$$\delta E_{\mathrm{Wig}}=-k_{\mathrm{B}}T\ln\left[\frac{\prod_{i}\sinh(x_{i}^{\mathrm{IS}})/x_{i}^{\mathrm{IS}}}{\prod_{i}\sinh(x_{i}^{\mathrm{TS}})/x_{i}^{\mathrm{TS}}}\right] \qquad \text{(S4)}$$

where the ratio of the ZPE to the thermal energy at each vibrational mode is $x_{i}^{\mathrm{IS/TS}}=h\nu_{i}^{\mathrm{IS}}/2k_{\mathrm{B}}T$. Taking the imaginary frequency mode into account, the quantum mechanical tunneling (QMT) effects can be considered by the Wigner tunneling correction.[16, 18]

Figure S15 presents the variations of the Mg diffusion barrier with respect to temperature when they migrate on a C_2N monolayer. The ZPE corrections of energy barriers (δE_{ZPE}) are in the range of 0.004 – 0.032 eV. The temperature dependent Wigner ZPE-corrected barriers ($\Delta E+\delta E_{\mathrm{Wig}}$) and temperature dependent Wigner ZPE-

and tunneling-corrected barriers ($\Delta E+\delta E_{\text{Wig/Tunn}}$) are determined, and they are located between the classical barrier (ΔE) and the ZPE corrected barrier ($\Delta E+\delta E_{\text{ZPE}}$). $\Delta E+\delta E_{\text{Wig}}$ and $\Delta E+\delta E_{\text{Wig/Tunn}}$ approach to $\Delta E+\delta E_{\text{ZPE}}$ at the low temperature limit while they reach ΔE (black line) at the high temperature limit. Figure S15 also showed that the QMT effect weakened as the temperature increases. The diffusion constants with and without QMT corrections are also provided in Table S2. And one can find that (1) the diffusion constants are promoted by the QMT effect, and (2) Mg has a two-stage diffusion behavior.

Section S5. Calculations of open circuit voltage (OCV)

We calculate the open circuit voltage (OCV) via the equation[19, 20] of $OCV=(E_{\text{C}_2\text{N}}+xE_{\text{Mg}}-E_{\text{Mg}_x\text{C}_2\text{N}})/xne$, where *e* is the electronic charge.

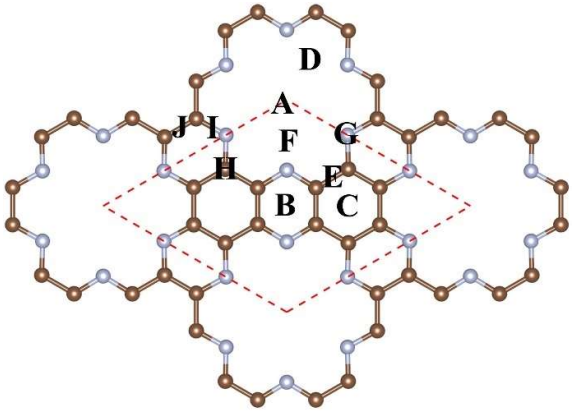

Figure S1. Schematic illustration of all possible positions of a single Mg atom adsorption on a C_2N monolayer.

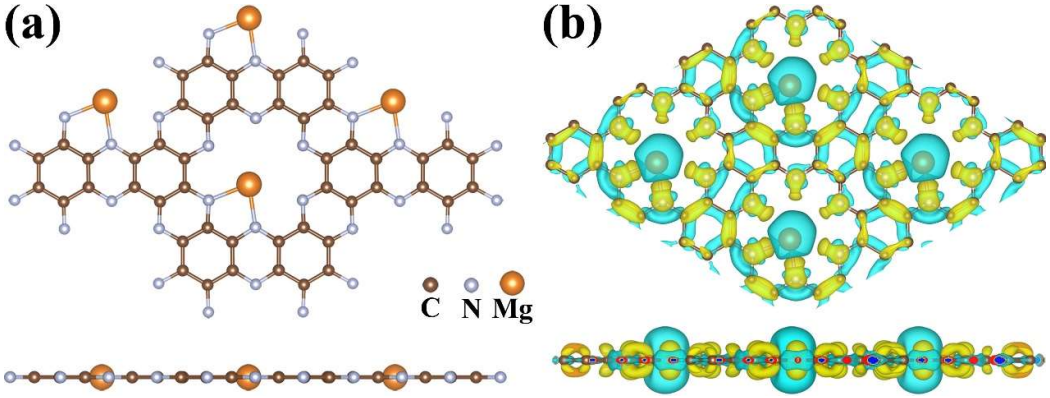

Figure S2. The most stable configuration (a) and charge density difference (b) of a single Mg atom adsorption on a C_2N monolayer. In charge density difference, cyan and yellow regions represent the charge depletion and accumulation, respectively.

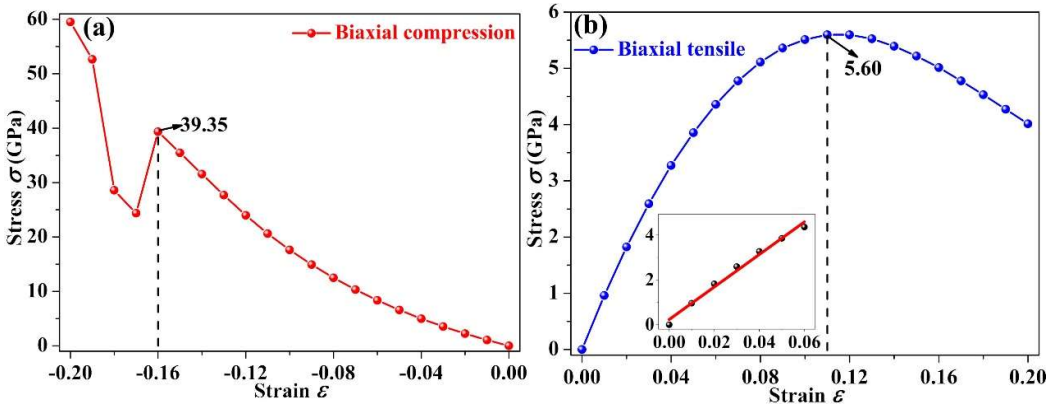

Figure S3. Calculated stress-strain curves of a C_2N monolayer under biaxial compression (a) and tensile (b) strains. The insert in (b) represents the fitting of the initial segment of stress-strain curve under biaxial tensile.

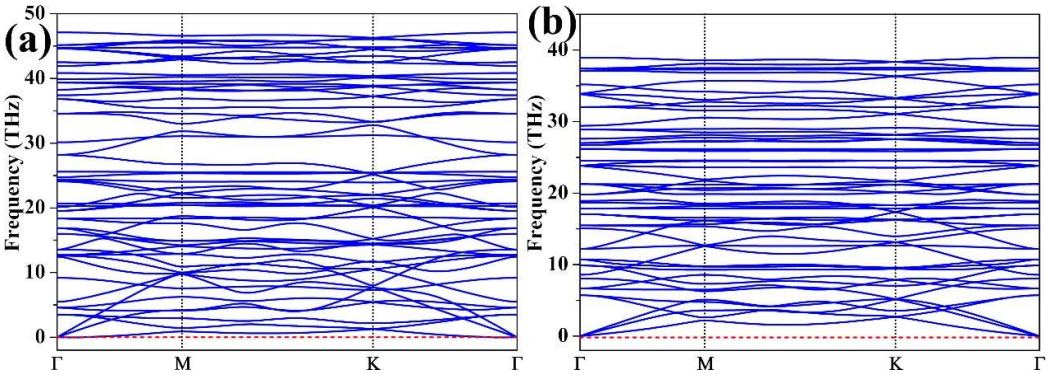

Figure S4. The phonon spectra of a pristine C_2N monolayer (a) and a strained C_2N monolayer under a biaxial tensile of 10% (b).

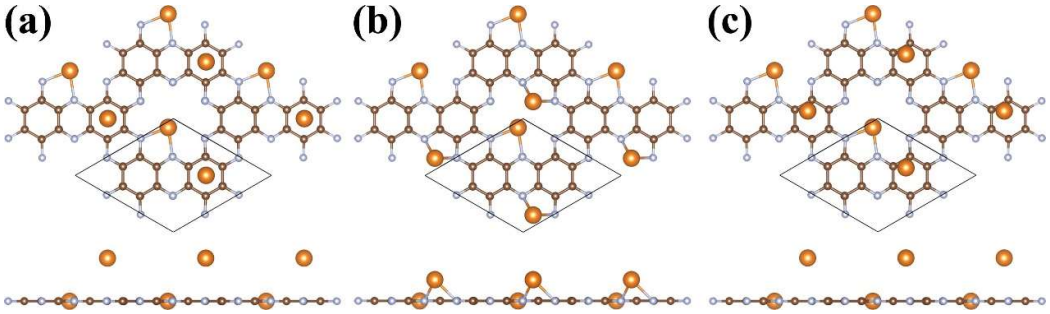

Figure S5. Top (upper) and side (below) views of optimized structures for the second Mg atom adsorption at C (a), D (b), and E sites (c) on a strain-free C_2N monolayer in the atom pair adsorption model.

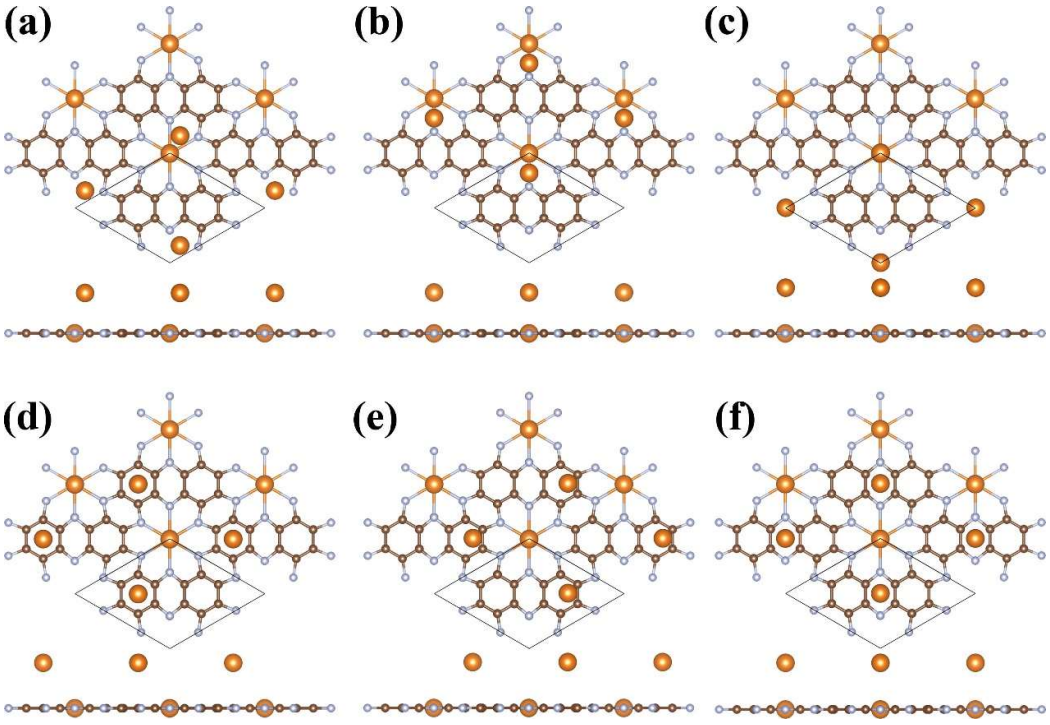

Figure S6. Top (upper) and side (below) views of optimized structures for the second Mg atom adsorption at D (a), F (b), A (c), C (d), E (e) and B sites (f) on a C_2N monolayer under a –10% biaxial compressive strain in the atom pair adsorption model.

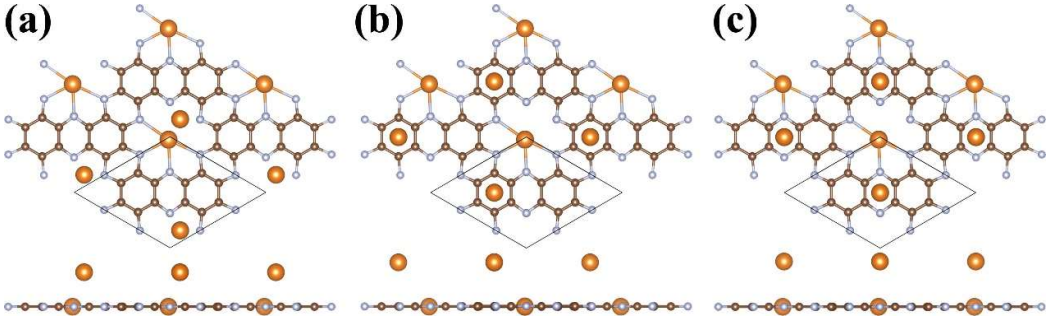

Figure S7. Top (upper) and side (below) views of optimized structures for the second Mg atom adsorption at D (a), C (b), and B (c) on a C_2N monolayer under a –5% biaxial compressive strain in the atom pair model.

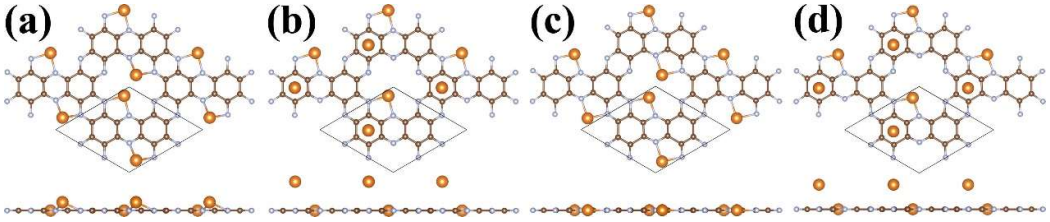

Figure S8. Top (upper) and side (below) views of optimized structures for the second Mg atom adsorption at D (a) and C sites (b) on a C_2N monolayer under a 5% biaxial tensile strain, and D (c) and C sites (d) under a 10% biaxial tensile strain in the atom pair adsorption model.

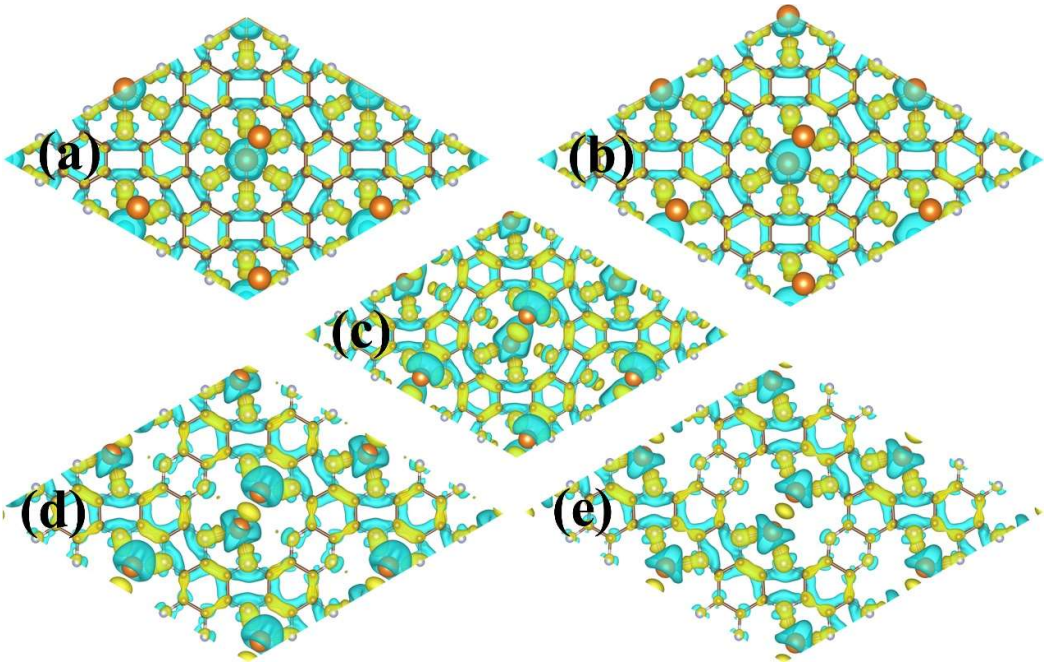

Figure S9. The charge density difference for the most stable configurations of two Mg atoms adsorption on a C_2N monolayer under biaxial strains of –10% (a), –5% (b), 0 (c), 5% (d), and 10% (e).

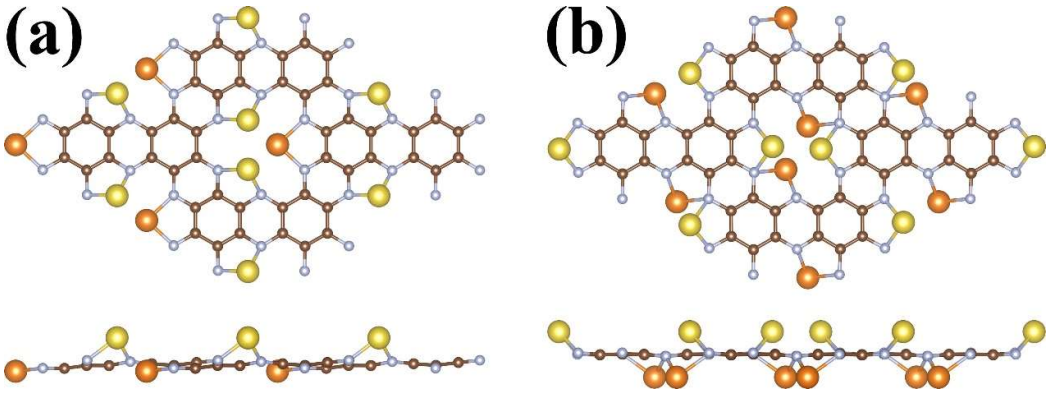

Figure S10. Top (upper) and side (below) views of the most stable configurations for three (a) and four (b) Mg atoms adsorption on a C_2N monolayer.

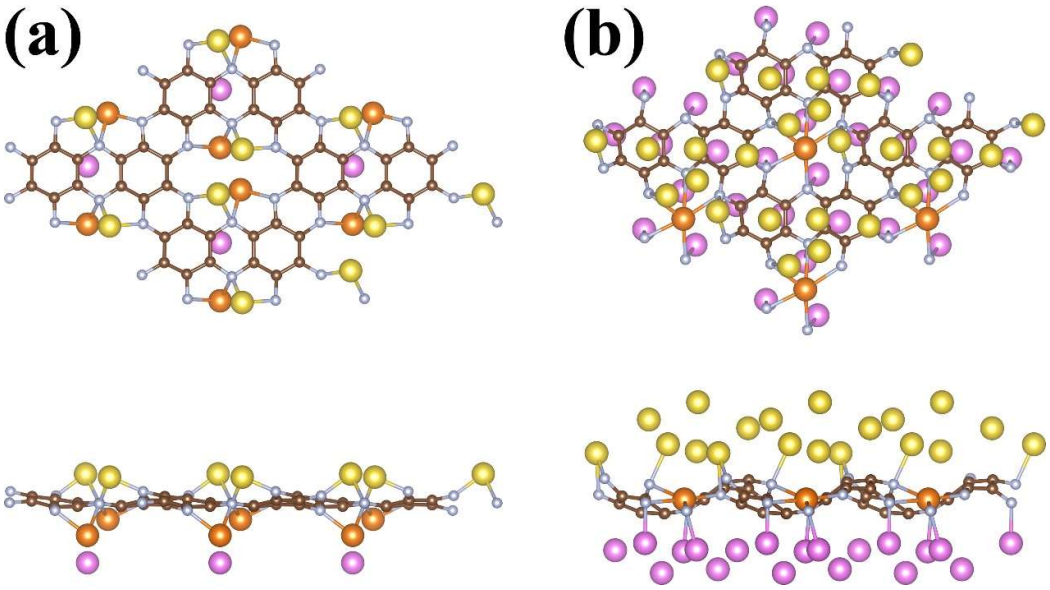

Figure S11. Snapshots of the most stable configurations of five (strain-free) (a) and thirteen (under –10% compressive strain) (b) Mg atoms adsorption on a C_2N monolayer at the end of a 5ps AIMD simulation under 300 K from top (upper) and side (below) views.

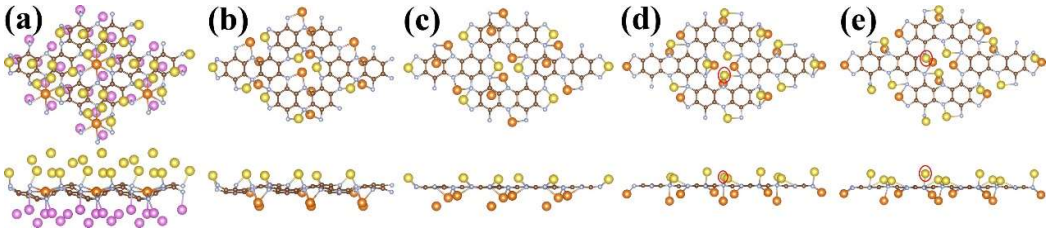

Figure S12. Top (upper) and side (below) views of the most stable configurations for the maximum Mg atoms adsorption on a C_2N monolayer under biaxial strains of –10% (a), –5% (b), 2% (c), 5% (d), and 10% (e).

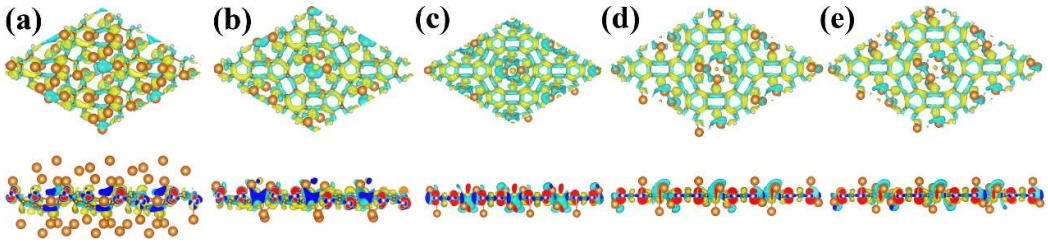

Figure S13. Top (upper) and side (below) views of charge density differences for the most stable configurations of the maximum Mg atoms adsorption on a C_2N monolayer under biaxial strains of –10% (a), –5% (b), 0 (c), 5% (d), and 10% (e).

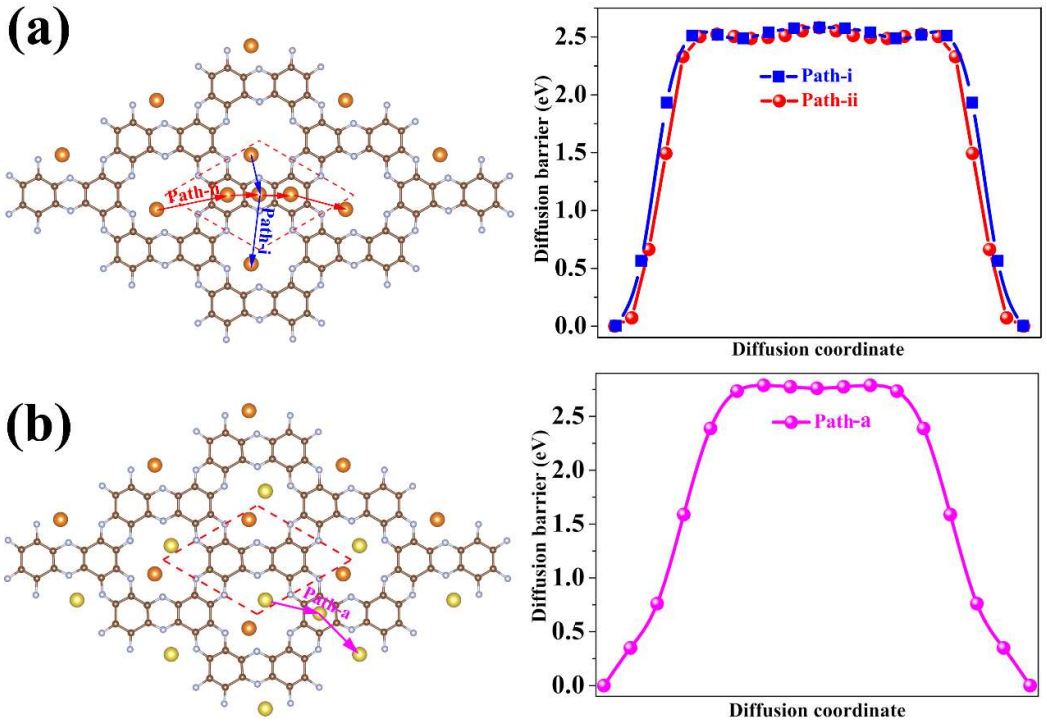

Figure S14. Diffusion paths and their corresponding energy barriers of a single (a) and two (b) Mg atoms diffusion on a C_2N monolayer under a biaxial tensile strain of 10%.

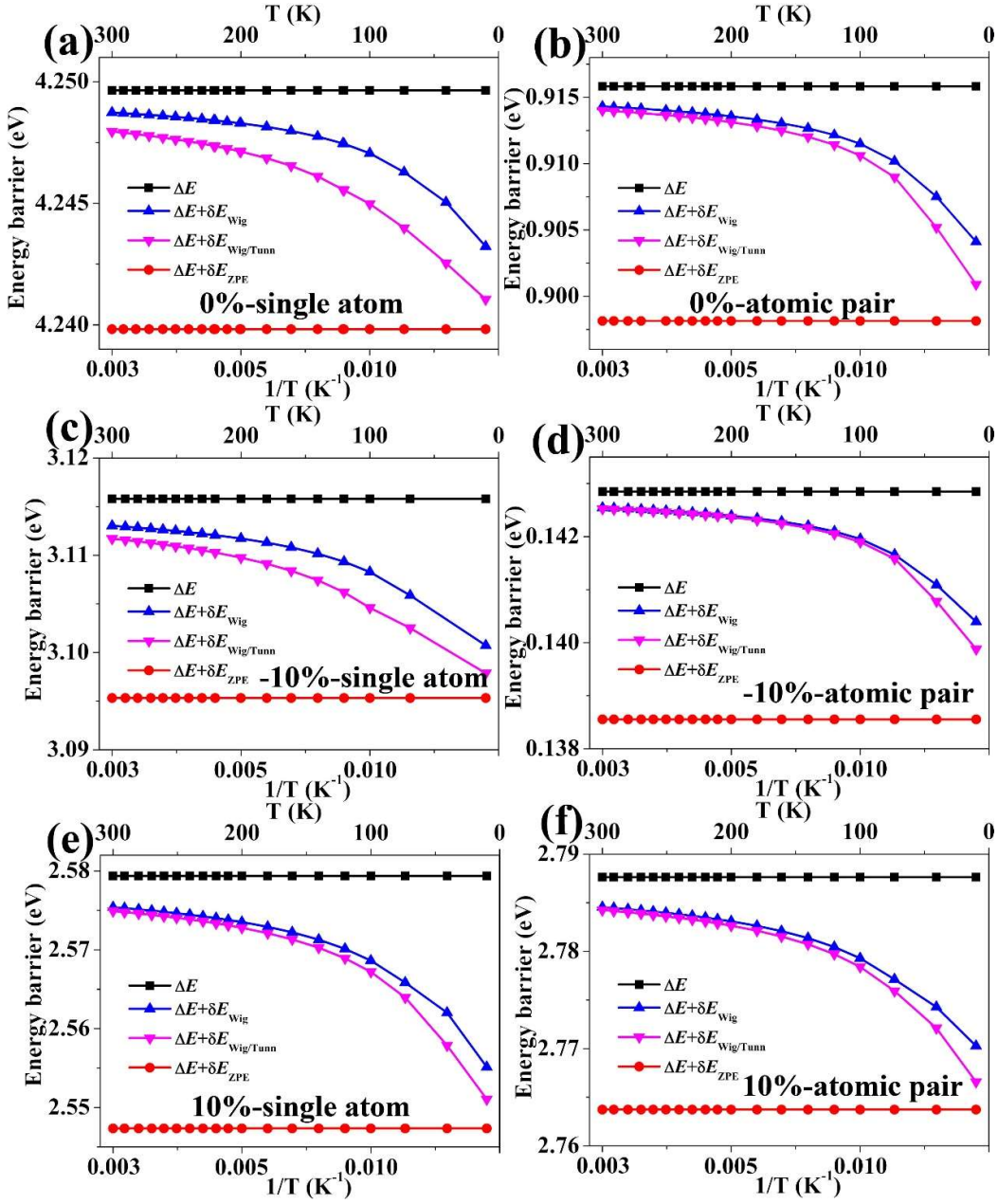

Figure S15. Variations of the classical energy barrier ΔE, ZPE-corrected barrier $\Delta E+\delta E_{ZPE}$, Wigner ZPE-corrected barrier $\Delta E+\delta E_{Wig}$, Wigner ZPE- and tunneling-corrected barrier $\Delta E+\delta E_{Wig/Tunn}$ with respect to temperature for a single Mg (a) and Mg atomic pair (b) diffusion on the pristine C_2N monolayers, for a single Mg (c) and Mg atomic pair (d) diffusion on the C_2N monolayers under biaxial compression of –10%, and for a single Mg (e) and Mg atomic pair (f) diffusion on the C_2N monolayers under biaxial tensile of 10%.

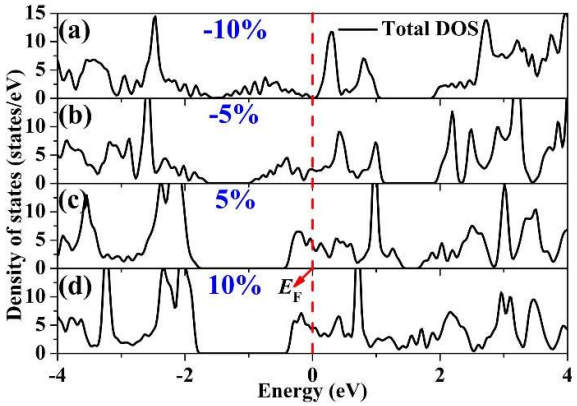

Figure S16. Total density of states for the most stable configurations of a single Mg atom adsorption on a C_2N monolayer under biaxial strains of –10% (a), –5% (b), 5% (c), and 10% (d). The Fermi level was set as 0 eV and labeled with a red vertical dash line.

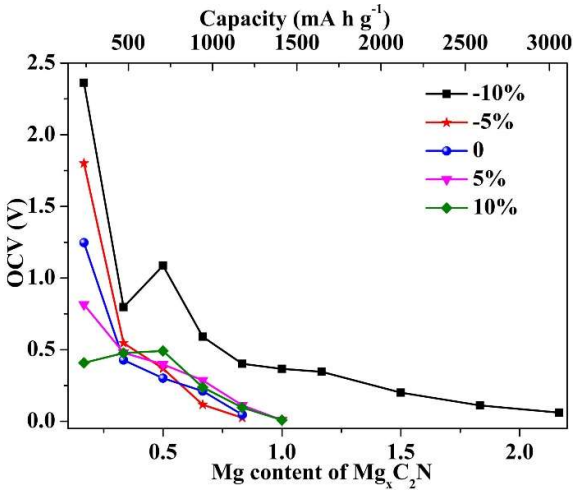

Figure S17. Open-circuit voltage profile versus concentration of Mg adatoms on a C_2N monolayer with and without strains.

Table S1. Adsorption energies E_{ads} (eV) of a single Mg atom adsorption on a C_2N monolayer with and without external strains. Total energies E_t (eV) of a C_2N monolayer with and without external strains. Bader charge (|e|) per Mg atom from a single Mg atom (B_{one}), from two Mg atoms in the atom pair approach (B_{two}) and from the maximum capacity (B_{max}) for a C_2N monolayer with and without external strains.

Strain	-10%	-5%	0	5%	10%
E_{ads}	-4.725	-3.601	-2.495	-1.629	-0.817
E_t	-147.5	-154.9	-157.1	-155.4	-151.2
B_{one}	1.706	1.697	1.680	1.649	1.630
B_{two}	0.922	0.942	1.033	0.994	0.966
B_{max}	1.081	0.788	0.776	0.803	0.818

Table S2. Classical diffusion constant k_c, Wigner ZPE- and tunneling-corrected diffusion constant $k_{Wig/Tunn}$, and percentages of tunneling effect (QMT) at 300 K of a single Mg (single atom) and of Mg atomic pair (atomic pair) diffusion on a C_2N monolayer without strain (0%) and under a biaxial compression (-10%) as well as under a biaxial tensile (10%).

System	k_{cl} (s^{-1})	$k_{Wig/Tunn}$ (s^{-1})	QMT (%)
0%-single atom	2.12×10^{-59}	2.26×10^{-59}	6.33
0%-atomic pair	1.41×10^{-02}	1.52×10^{-02}	6.80
10%-single atom	5.02×10^{-30}	5.97×10^{-30}	15.88
10%-atomic pair	2.61×10^{-34}	2.97×10^{-34}	12.26
-10%-single atom	3.90×10^{-40}	4.57×10^{-40}	14.60
-10%-atomic pair	9.01×10^{9}	9.12×10^{9}	1.27

References

1. P. E. Blöchl, *Phys. Rev. B*, 1994, 50, 17953.
2. J. P. Perdew, K. Burke and M. Ernzerhof, *Phys. Rev. Lett.*, 1996, 77, 3865-3868.
3. G. Kresse and J. Furthmüller, *Phys. Rev. B*, 1996, 54, 11169.
4. S. Grimme, J. Antony, S. Ehrlich and H. Krieg, *J. Chem. Phys.*, 2010, 132, 154104.
5. G. Henkelman, B. P. Uberuaga and H. Jónsson, *J. Chem. Phys.*, 2000, 113, 9901-9904.
6. M. Yu and D. R. Trinkle, *J. Chem. Phys.*, 2011, 134, 064111.
7. J. Liu, S. Wang and Q. Sun, *P. Natl. Acad. Sci. USA*, 2017, 114, 651.
8. Z. Guo, J. Zhou, C. Si and Z. Sun, *Phys. Chem. Chem. Phys.*, 2015, 17, 15348-15354.
9. Q. Peng and S. De, *Phys. Chem. Chem. Phys.*, 2013, 15, 19427-19437.
10. C. Lee, X. Wei, J. W. Kysar and J. Hone, *Science*, 2008, 321, 385-388.
11. J. H. Los, J. M. H. Kroes, K. Albe, R. M. Gordillo, M. I. Katsnelson and A. Fasolino, *Phys. Rev. B*, 2017, 96, 184108.
12. S. Zhang, J. Zhou, Q. Wang, X. Chen, Y. Kawazoe and P. Jena, *Proc Natl Acad Sci USA*, 2015, 112, 2372-2377.
13. C. Wert and C. Zener, *Phys. Rev.* , 1949, 76, 1169-1175.
14. G. Henkelman, A. Arnaldsson and H. Jónsson, *J. Chem. Phys.* , 2006, 124, 044706.
15. S. Karmakar, C. Chowdhury and A. Datta, *J. Phys. Chem. C*, 2016, 120, 14522-14530.
16. S. Guo, X. Hu, W. Zhou, X. Liu, Y. Gao, S. Zhang, K. Zhang, Z. Zhu and H. Zeng, *J. Phys. Chem. C*, 2018, 122, 29559-29566.
17. E. Wigner, *Trans. Faraday Soc.*, 1938, 34, 29-41.
18. E. Wigner, *Z. Phys. Chem., Abt. B*, 1932, 19, 203-216.
19. B. Xiao, Y. C. Li, X. F. Yu and J. B. Cheng, *ACS Appl. Mater. Interfaces*, 2016, 8, 35342-35352.
20. D. Wang, Y. Liu, X. Meng, Y. Wei, Y. Zhao, Q. Pang and G. Chen, *J. Mater. Chem. A*, 2017, 5, 21370-21377.